Paper

IJASS

International Journal of
Aeronautical and Space Sciences

Multi-Point Aerodynamic Design Optimization of DLR F-6 Wing-Body-Nacelle-Pylon Configuration

Takashi Saitoh*

Department of Aerospace Engineering, Tohoku University, Sendai 980-8577, Japan

Hyoungjin Kim**

Department of Mechanical Engineering, Kyung Hee University, Yongin 17104, Republic of Korea

Keizo Takenaka* and Kazuhiro Nakahashi*****

Department of Aerospace Engineering, Tohoku University, Sendai 980-8577, Japan

Abstract

Dual-point aerodynamic design optimization is conducted for DLR-F6 wing-body-nacelle-pylon configuration adopting an efficient surface mesh movement method for complex junction geometries. A three-dimensional unstructured Euler solver and its discrete adjoint code are utilized for flow and sensitivity analysis, respectively. Considered design conditions are a low-lift condition and a cruise condition in a transonic regime. Design objective is to minimize drag and reduce shock strength at both flow conditions. Shape deformation is made by variation of the section shapes of inboard wing and pylon, nacelle vertical location and nacelle pitch angle. Hicks-Henne shape functions are employed for deformation of the section shapes of wing and pylon. By the design optimization, drag coefficients were remarkably reduced at both design conditions retaining specified lift coefficient and satisfying other constraints. Two-point design results show mixed features of the one-point design results at low-lift condition and cruise conditions.

Key words: Unstructured grid, Aerodynamic design optimization, Adjoint method, Multi-point design

1. Introduction

In three-dimensional aerodynamic shape design optimization, complex geometries such as wing-body-junctions, integration of engine with pylon and nacelle still pose difficulties. For design modification of these configurations with body-installation junctions, junction lines need to be redefined, and surface and volume meshes should be regenerated or moved both on the wing and body.

For automated aerodynamic shape design of the junction region, overset-grid methods can be applied with relative ease.[1, 2] Another approach is direct link of a design tool and CAD system [3], which requires regeneration of surface and volume mesh when a surface geometry is newly modified. As an alternative way, Murayama et al. [4] developed a surface mesh movement method adopting a surface mapping method in which a three-dimensional surface mesh region to be moved is partially cut out to make a patch and mapped onto a two-dimensional parametric domain. Mesh points on the parameter domain are then moved appropriately and transformed back to the three-dimensional physical domain. For design problems the patch map and relating surface mesh should be regenerated in each design cycle. This may cause inefficiency for whole design procedure.

Kim and Nakahashi [5] proposed a novel surface mesh movement method for aerodynamic design of body-installation junctions. In the method, instead of mapping the surface mesh to a parametric patch mesh, surface mesh

---

(cc) * Graduate Student
  ** Professor, Corresponding author: Hyoungjin.Kim@khu.ac.kr
  *** Graduate Student
  **** Professor

points directly move on curved body surfaces by using a surface recovery method. Neither CAD-interface nor new mesh regeneration is required. In this study, we apply the direct surface mesh movement method of Ref.[5] to aerodynamic design optimization of complex configuration with junctions.

Among several design optimization methods applicable to aerodynamic shape design problems, gradient-based methods have been used widely due to its well developed numerical algorithm and relatively small computational burden. In the application of gradient-based methods to practical aerodynamic design problems, one of major concerns is accurate and efficient calculation of sensitivity gradient of aerodynamic objective function. During the last decade, the adjoint method has grown much attention as an efficient sensitivity analysis method for aerodynamic optimization because it allows calculation of sensitivity information independently of the number of design variables. [6]

In our previous study, the surface mesh movement method was coupled with a gradient-based design optimization method. [7] For the flow and sensitivity analysis, an unstructured finite volume Euler solver and its discrete adjoint code was utilized. The coupled design system was applied to design examples on complex configuration with junctions such as ONERA-M5 and DLR-F6 WBNP (wing-body-nacelle-pylon) configurations. The DLR-F6 configuration was designed at low-lift off-design condition, which emerged at climb or descent in a flight envelope. Although aerodynamic performances have been remarkably improved at the design point, performances at other flow conditions might have been degenerated or could be improved further. The objective of the present study is to conduct a single-point design at a cruise condition and dual-point designs of at cruise and low-lift condition on the DLR-F6 wing-body-nacelle-pylon configuration.

The remaining of this paper is composed as follows: In Section 2, the direct surface mesh movement methodology for junction treatment is briefly explained. Design procedures including flow/adjoint analysis, optimization method and sequence of design iteration are described in Section 3. Design results of single and dual-point designs are given in Section 4. Finally conclusions are made in Section 5.

2. Junction Treatment

In this section some brief information on the surface mesh movement method for junction treatment proposed in Ref.[5] is presented for completeness. More details on the

surface mesh movement can be found in Ref. [5].

2.1 General Procedure

Figure 1 shows a schematic diagram for a wing-fuselage configuration in which both wing and fuselage geometry are assumed to be modified by design. Solid lines represent initial geometry and dotted lines modified geometry. Taking a wing-fuselage design problem as an example, the procedure can be briefly described as follows:

1) Modify geometries of wing and fuselage.
2) For the modified geometries, find the new location of the wing-fuselage junction nodes. Calculate geodesic distances from initial to new junction nodes along the faceted surface.
3) With the body-fuselage junction node movements as boundary conditions, move wing surface mesh points along the faceted surfaces using a two-dimensional spring analogy based on the geodesic distances.
4) Conduct the same process as Step 3 for fuselage surface mesh points.
5) Project new surface mesh points on the faceted surfaces to the smooth surface by a surface recovery method with the initial mesh as background mesh.
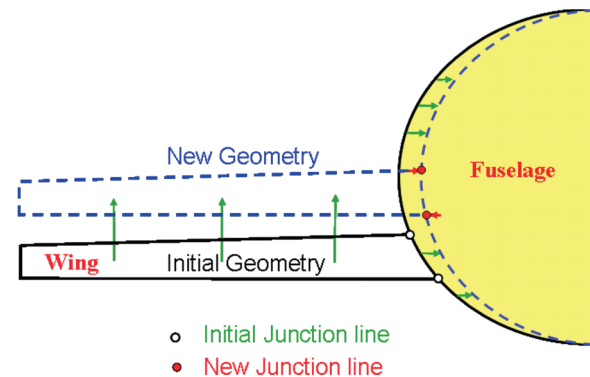6) Modify the volume mesh according to the new surface mesh.

Fig. 1. Schematic diagram for geometry modification with wing-body juncture

2.2 Finding New Junction Location

In order to find a new position of juncture nodes, wing surface geometry needs to be extrapolated spanwisely when undefined wing geometry inside the fuselage is exposed by the geometric modification. For structured grids, spanwise mesh lines on a wing surface can be easily used for the extrapolation. On the other hand, unstructured meshes do not have such aligned mesh lines. Therefore at every junction nodes one need to calculate an extrapolating vector
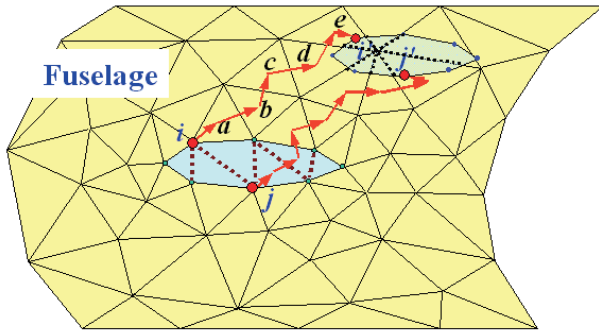
Fig. 2. Neighbor-to-neighbor search from initial to new junction location (Subsidiary cells are added by the edges in dotted lines)

which is along local sweep angle and tangential to wing surface cell adjacent to the juncture. The next step is to find an intersection point where the extrapolation vector meets the fuselage surface, which is conducted using a neighbor-to-neighbor jump search method. (See Fig. 2)

Although the neighbor-to-neighbor search enables an efficient one-dimensional search, it may fail to reach to the target point if there is a hole between the initial and target points. This is the case for the node j on the lower juncture line in Fig. 2. In order to circumvent this problem subsidiary surface cells are added in the junction hole as shown in dotted lines. The subsidiary cells are also helpful to recover fuselage geometry on the hole by a surface recovery method.

2.3 Surface Mesh Movement

When a new junction point is found by the neighbor-to-neighbor search method, one need to calculate the geodesic distance between the initial and new junction points which is used as boundary conditions for surface mesh movement. Geodesic distance is distance between the points along curved surface. Euclidian distance is a good approximation to the geodesic distance only at short ranges and regions of small curvature. Although Euclidian distance is much simpler to compute, the geodesic distance would give more robust results because the distance actually traveled by surface nodes is geodesic distance which is longer than Euclidian distance on curved surfaces. If Euclidian distance is used for the surface mesh movement problem, one might obtain flipped surface meshes because of comparatively larger movement of junction nodes than inner surface nodes.

3. Design Tools

The junction treatment method described in Section 2 is coupled with existing aerodynamic design optimization

tool [9, 10] composed of an unstructured flow solver, a discrete adjoint code, gradient-based optimizers, and mesh modification routines.

3.1 Flow and Sensitivity Analysis

A three-dimensional unstructured Euler solver [11] was used for flow analysis in order to get a fast turnaround time. The governing Euler equations are solved by a finite volume cell-vertex scheme. The control volumes are non-overlapping dual cells constructed around each cell node. Each edge connecting two nodes is associated with vector area of control surface, and gas dynamic fluxes are computed through the areas. Primitive gas dynamic variables are linearly reconstructed inside the median-dual control volume for second order spatial accuracy and multiplied by a limiter function for monotonicity preservation. After the reconstruction, a flux quadrature is performed around each control volume using a single point along each face of the control volume. The flux is computed by an approximate Riemann solver. For the time integration, Lower-Upper Symmetric Gauss Seidel (LU-SGS) implicit method is adopted [12].

For efficient calculation of sensitivity information, a discrete adjoint solver developed from the flow solver described above is used. [9] The discrete adjoint solver utilizes the same time integration method as the flow solver. By the use of the adjoint method, computational cost for sensitivity analysis is independent of the number of design variables.

3.2 Drag Calculation Method

There are three approaches in the drag force calculation of aerodynamic configurations: near-, far- and mid-field approaches. The near field approach calculates drag force on aerodynamic configurations by integrating pressure and skin friction forces on the body surfaces. The far-field approach allows the breakdown of the total drag amount into its physical causes such as vortex (induced) drag and entropy drag components. However, because the integration is performed far from the aerodynamic bodies, the artificial or the spurious drag contributions cannot be identified. The mid-field method conducts the integration of the drag components in the region close to the body where actual drag sources such as entropy production occur. Therefore, in addition to the induced drag, more specific entropy drag components such as viscous and wave drag terms can be calculated. The spurious drag can also be identified in addition to the physical or "pure" drag components. In the present study, a mid-field drag decomposition method [8] is

employed for accurate calculation of the physical pure drag components for the design results.

3.3 Optimization Algorithms

In this study, we adopt a gradient-based optimization method utilizing of an objective function gradient provided by the adjoint solver. We use the Sequential Quadratic Programming (SQP) method [13] in which the objective function is approximated by a quadratic Taylor series expansion to create a direction-finding problem. Detailed algorithms and methodologies of the SQP method are described in Ref.13.

3.4 Design Procedure

Figure 3 shows the general design procedure in this study. With an objective function and its gradient information computed by flow and adjoint analysis, an optimizer finds new set of design variables for a local optimum solution along the search direction. New surface geometry is then constructed following the design variables. If juncture regions are modified by the design, the juncture treatment procedure described in Section 2 is applied to get a new surface geometry with neither CAD intervention nor time-consuming remeshing process of surface and volume meshes during the design cycle. For the modified surface mesh, volume mesh is also modified accordingly. In this study, volume mesh is modified by a robust volume mesh modification method based on a torsion spring analogy proposed by Murayama et al. [4]. With the newly modified meshes, flow analysis is conducted to calculate objective function of the design problem. Then adjoint analysis is conducted if necessary. This design iteration is repeated within user-specified maximum iteration number until reduction amount of the objective function becomes negligible.
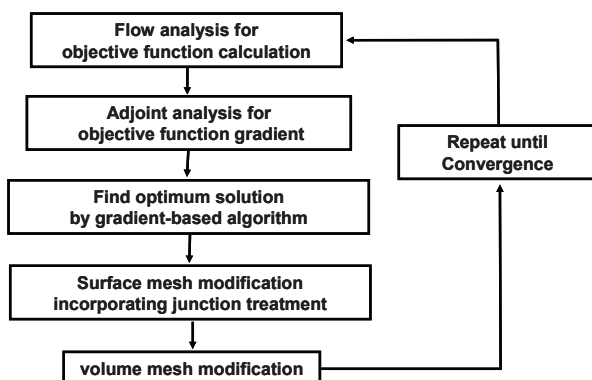

Fig. 3. Flow chart of design procedure

4. Design Results

Installation of nacelle, pylon and engine components has significant effects on aircraft performances especially at high speed flows. There have been several experiments and theoretical investigations on the topic of these aerodynamic interference effects [14]. The present design methodology can be a powerful tool for aerodynamic design of complex aircraft configurations with junction interference effects. As a design example of an aircraft configuration with wing-nacelle-pylon interference, here we apply the present method to DLR-F6 WBNP (wing-body-nacelle-pylon configuration). Computational mesh for the configuration is shown in Fig. 4 containing 463,846 nodes and 2,565,463 tetrahedral. The surface mesh is generated by the direct advancing front method coupled with the geometrical feature extraction on the STL (Stereolithography) data format. [15] The tetrahedral volume mesh is generated by a Delaunay-type generation method. [16]
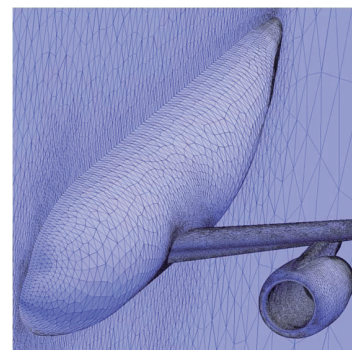

Fig. 4. Computational mesh for DLR-F6 configuration

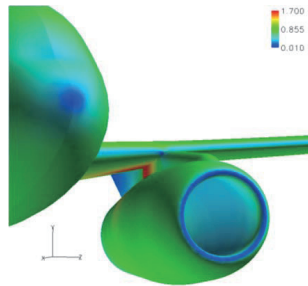### 4.1 Definition of Design Problem: Single-Point Design

Flow conditions for the first design condition are freestream Mach number of 0.74 and C_L of 0.14, which correspond to a critical condition for climb or descent and is referred to as a low lift condition in this study. At the low-lift condition, flow over initial pylon surface is highly accelerated because of the interference of wing, nacelle and pylon as shown in Fig. 5(a). The pylon surface Mach number reaches up to 1.72 leading to a strong shock wave, which may cause a buffet. Buffet is a shock-boundary layer interaction phenomenon causing shock wave oscillation and subsequent oscillation of lift and pitching moment. In transonic regimes, buffet is a major limiting factor for the cruise speed and lift. Objective of the design at the low-lift condition is to minimize drag and eliminate the strong shock wave on the pylon to reduce the buffet risk.

Flow condition is Mach number of 0.74 and C_L of 0.54 corresponding to a cruise condition. At the cruise condition, the strong shock wave on the pylon, which occurred at the low-lift condition, does not appear. Although flow over the initial pylon is accelerated up to Mach 1.3 because of the interference of wing, nacelle and pylon, there is no strong shock wave on the pylon surface. At this condition, however, there occurs a shock wave on the upper wing surface as can be seen in Fig. 5(b). Especially, flow acceleration around leading edge region is much stronger on the inboard wing than that of the outboard wing, as shown in the 'Δ shape' region at the inboard leading edge region having Mach number larger than 1.4 in Fig. 5(b) because of the interference effect of wing, nacelle and pylon. Design target at the cruise design condition is to minimize drag by reducing the shock wave strength on the upper surface of the inboard wing.
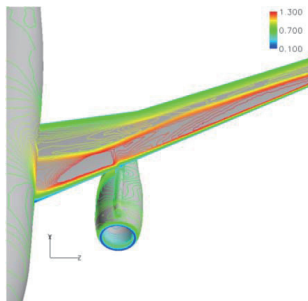
Design constraints for the designs are imposed as follows:
1) No buffet on the pylon surface for the low-lift condition only
2) $C_L \geq C_L^*$ (= initial C_L)
3) Wing section maximum thickness ≥ Initial wing section maximum thickness(@34%chord)
4) Pylon section maximum thickness ≥ Initial pylon section maximum thickness(@25%chord)

The constraint of buffet suppression is implemented by imposing upper bound of surface Mach numbers as 1.3 on the pylon. This constraint is treated as a penalty term added to the objective function F as follows.

$$\mathrm{F} = C_D + k \sum_{surface} max(0, p_{lim} - p_{surf}), \tag{1}$$

where k is a weighting factor multiplied to the penalty term, and p_{lim} is pressure limit calculated from the Mach number of 1.3 by the isentropic relation, p_{surf} is local pressure on pylon surface. Local pressure values are constrained instead of local Mach numbers for simplicity in differentiation of the objective function in adjoint formulation. [17] If the lift constraint is dealt as an explicit constraint in the optimization procedure, it requires an additional adjoint analysis for the calculation of gradient of C_L per each design cycle. In this study, therefore, the lift constraint is satisfied running the flow solver in a fixed-lift mode, in which the angle of attack is adjusted on the fly based on $C_L\alpha$. The modified objective function considering the lift constraint is given as follows. [11]

$$F_{new} = F - \frac{c_{D_\alpha}}{c_{L_\alpha}}(C_L - C_L^*), \tag{2}$$

where the second term in the right-hand side containing lift coefficients acts as a penalty term which prevents the design from reducing the drag by simply reducing the lift. Geometric constraints such as wing and pylon section thickness constraints are treated as explicit constraints in the SQP method.

4.2 Definition of Design Problem: Dual-Point Design

For dual-point designs, objective function F is defined as a weighted average of the objective functions at the design conditions as follows:

$$\mathrm{F} = wF_1 + (1-w)F_2, \tag{3}$$

where F_1 and F_2 are the objective function defined at each design condition, and w is a weighting factor. Constraints are the same as the single-point designs.

4.3 Surface Geometry Modification

Geometry modifications are made by inboard wing section shape deformation, pylon section shape deformation, nacelle vertical movement, and nacelle pitch angle variation. As shown in Fig. 6(a), we use three design sections along the inboard wing span. Wing-pylon junction is also used as a design section for pylon geometry perturbation. (See Fig. 6(b)) The inboard wing and pylon section geometries are modified by adding a linear combination of Hicks-Henne shape functions [18]. On each of the four design sections 20 design variables are defined for Hicks-Henne shape functions. With the new geometry at the design sections,

(a) Mach contours at the low-lift condition (C_L=0.14)

(b) Mach contours at the cruise condition (C_L=0.54)

Fig. 5. Flow analysis for the initial DLR-F6 WBNP configuration (M_∞=0.74)

node points on the inboard wing surface and pylon surface are linearly interpolated independently. Then the surface mesh movement approach presented in Ref. [5] and also briefly described in Section 2 is applied to the wing-pylon junction region. In addition to the 80 design variables for the design sections, vertical movement and pitch angle variation of nacelle are also considered as design variables. Thus the number of design variables is 82 in all.

Regarding the nacelle movements, pylon geometry is deformed accordingly with fixed nacelle-pylon and wing-pylon junctions. Pylon deformation can be conducted by a simple spring analogy with spring constant based on edge length. Boundary conditions for the pylon deformation are imposed as follows: displacement of pylon-wing junction points as zero, displacement of pylon-nacelle junction points as the nacelle displacement, and pylon leading and trailing edges are linearly interpolated from the lower and upper boundaries based on x coordinate. Refer to Ref.[5] for more details on the pylon deformation.

4.4 Single Point Design Results

4.4.1 Low lift condition

In our previous study, a design at the low-lift condition was already conducted [7]. By the design procedure, total drag coefficient was reduced by 16 counts form the initial value (Table 1). As shown in Table 1, the pure drag coefficient is reduced by 15 counts, and the wave drag is reduced by 15 counts (-97.0%), which stands for almost all the drag reduction in total and pure drag. The difference between the

total drag and pure drag shows spurious drag, which is non-physical drag caused by numerical dissipation. [8]

Figure 7 shows Mach contours of initial and design configurations. The strength of shock wave on the wing lower surface and pylon surface has been remarkably reduced. It can also be noted from Fig. 8 and Fig. 9 that the flow acceleration on the pylon is remarkably reduced by the design to remove the shock. Table 2 shows a performance of the low-lift design configuration at the cruise condition, where the total drag coefficient is increased by 2 counts from that of the initial configuration by the pure drag remains the same as the initial configuration.

4.4.2 Cruise condition

Table 3 summarizes the single-point design results at the cruise condition. The lift is kept at the initial value by perturbing the angle of attack. The wave drag coefficient is reduced by 6 counts, which is a dominant share of the pure drag reduction. Table 4 shows aerodynamic coefficients of single point cruise design at the low-lift condition. The pure drag coefficient is reduced by 8 counts form the initial value.

Figure 9 show Mach contour and shock visualization on the wing upper surface of the cruise design, from which it can be noted that the strength of shock wave on the inboard wing upper surface is remarkably reduced through the design procedure. On the outboard wing upper surface, it seems that the shock strength is reduced because of the nacelle movement and spanwise effect of the inboard wing section design. Flow acceleration on the pylon is also reduced. (Fig. 10). Fig. 11 compares wing shape and pressure distributions
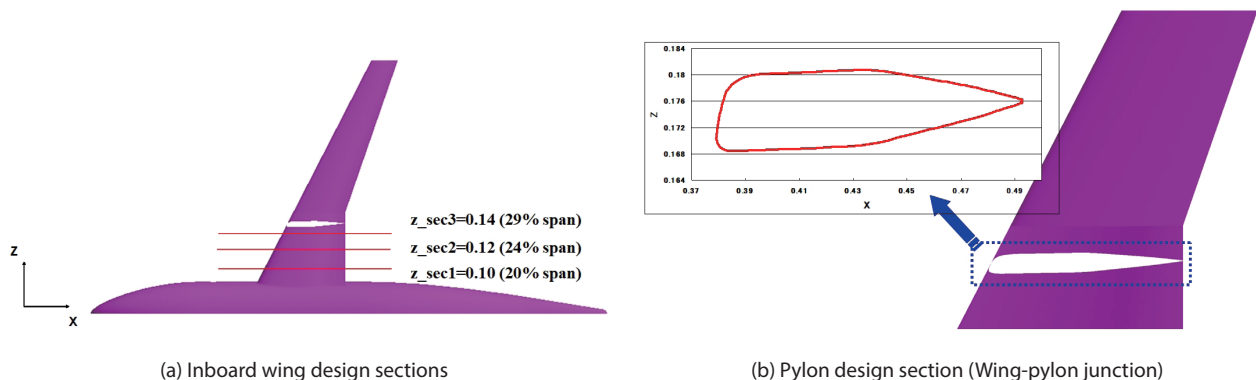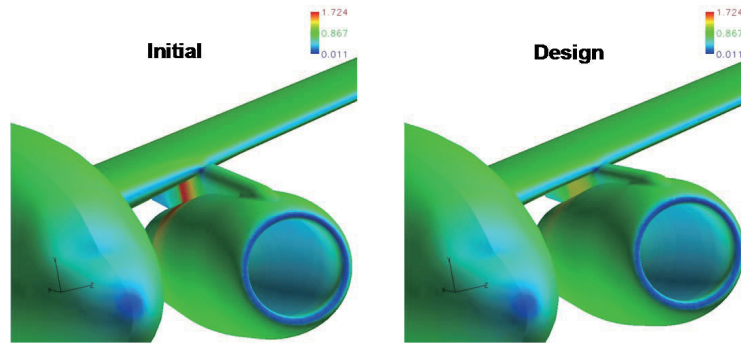

(a) Inboard wing design sections

(b) Pylon design section (Wing-pylon junction)

Fig. 6. Design sections for DLR-F6

Table 1. Single-point Design Results at the low-lift condition

	C_L	C_{D_TOTAL}	C_{D_PURE}	C_{D_WAVE}
Initial	0.1402	0.0080	0.0075	0.00150
Design	0.1401	0.0064	0.0060	0.00004
Diff. counts (%)	-1 (-0.02%)	-16 (-20%)	-15 (-20%)	-15 (-97%)

(a) Mach contours on DLR-F6 Wing-Body-Nacelle-Pylon surfaces [7]

Initial   Design
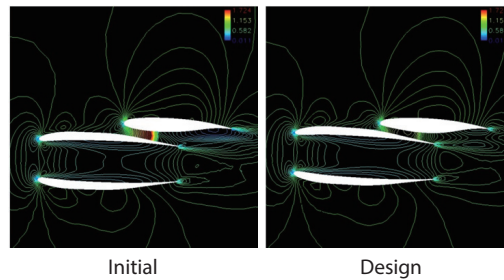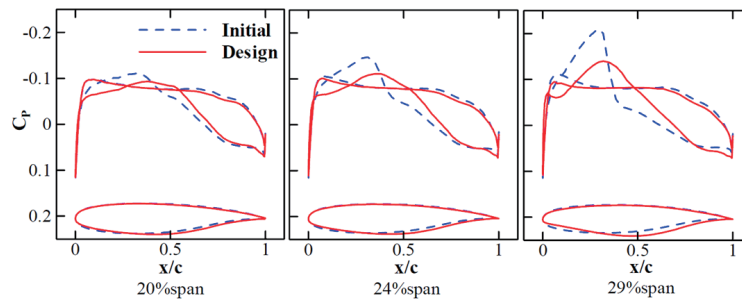
(b) Mach contours at 34% span section of DLR-F6

Fig. 7. Single-point design results at the low-lift condition (M∞=0.74, C_L=0.14) [7]

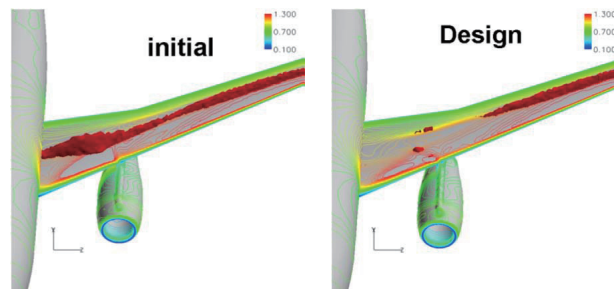Fig. 8. Single-point design results at the low-lift condition: Wing section shapes and pressure distributions

Fig. 9. Single point design results at the cruise condition (M∞=0.74, C_L=0.54): Surface Mach contours and shock wave visualization

Table 2. Aerodynamic coefficients of the single-point low-lift design at the cruise condition

	C_L	C_{D_TOTAL}	C_{D_PURE}	C_{D_WAVE}
Initial	0.5401	0.0227	0.0187	0.0015
Design	0.5401	0.0229	0.0187	0.0015
Diff. counts (%)	0 (0 %)	+2 (+0.8%)	0 (0%)	0 (0%)

Table 3. Single-point Design Results at the cruise condition

	C_L	C_{D_TOTAL}	C_{D_PURE}	C_{D_WAVE}
Initial	0.5401	0.0227	0.0187	0.0015
Design	0.5400	0.0220	0.0181	0.0009
Diff. counts (%)	-1 (-0.02%)	-7 (-3.1%)	-6 (-3.2%)	-6 (-40.7%)

Table 4. Aerodynamic coefficients of the single-point cruise design at the low-lift condition

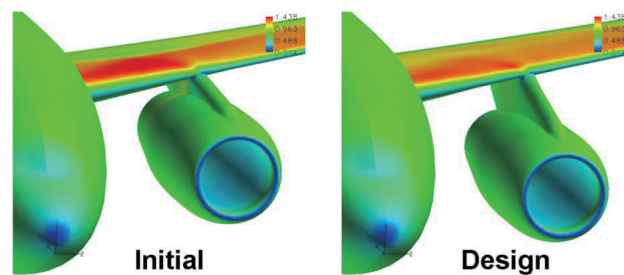|	C_L	C_{D_TOTAL}	C_{D_PURE}	C_{D_WAVE}
Initial	0.1402	0.0080	0.0075	0.0015
Design	0.1400	0.0071	0.0067	0.0007
Diff. counts (%)	-2 (-1.4 %)	-9 (-11.2%)	-8 (-9.3%)	-8 (-53.3%)

Fig. 10. Single point design results at the cruise condition: Mach contour on DLR-F6 Wing-Body-Nacelle-Pylon surfaces
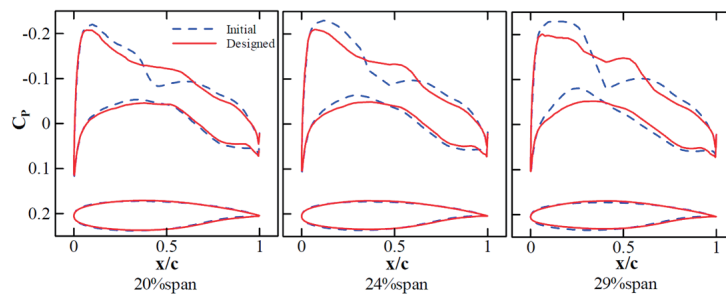

Fig. 11. Single point design results at the cruise condition: Wing section shapes and pressure distributions

at the design sections. Section pressure distributions also show that the shock strength on the wing upper surface has been remarkably reduced. At the initial configuration, there is strong flow acceleration area like a Δ shape on the leading edge of the inboard wing upper surface near the wing-pylon junction. The deformation of the wing shapes change the flow field on the configuration, and downward nacelle movement makes the channel area between the nacelle and wing wide. These effects of the design reduce the wave drag.

4.4.3 Dual point design for low-lift and cruise conditions

Table 5 summarizes results of a dual-point design considering the low-lift and cruise conditions with a weighting factor w=0.5. By the design process, the pure drag coefficient is reduced by 12 counts at the low-lift condition

and by 6 counts at the cruise condition. The wave drag is also reduced at each condition. At the low-lift condition, wave drag is reduced by 14 counts. Fig. 12 shows Mach contours at the low-lift condition and nacelle vertical deformation of the dual-point design. The strong shock on pylon is reduced remarkably. The movement and pitch down of the nacelle widens the area between the nacelle and wing to weaken the interference effect. Fig. 13 shows that the strong flow acceleration and shock wave are reduced. And wing section shape deformation makes acceleration area move to the leading edge. It can be noted from the section pressure distributions in Fig.14 and Fig.15 that the strength of shock wave is remarkably reduced through the design procedure, which can also be confirmed in Fig. 16 where visualization of shock wave is provided.

Table 5. Dual point design results with $w = 0.5$

Case		C_L	C_{D_TOTAL}	C_{D_PURE}	C_{D_WAVE}
	Initial	0.1402	0.0080	0.0075	0.0015
Low-lift	Design	0.1402	0.0068	0.0063	0.0001
	Diff. counts (%)	0 (0 %)	-12 (-15%)	-12 (-16%)	-14 (-91%)
	Initial	0.5401	0.0227	0.0187	0.0015
Cruise	Design	0.5401	0.0216	0.0181	0.0008
	Diff. counts (%)	0 (0%)	-11(-5%)	-6 (-3%)	-7 (-46%)

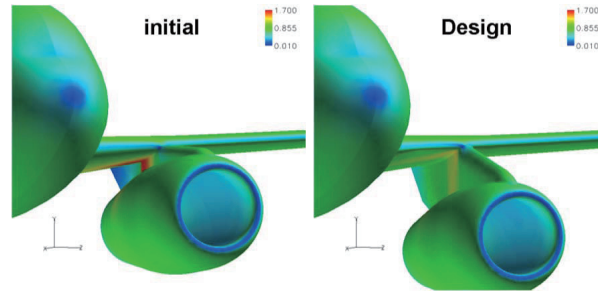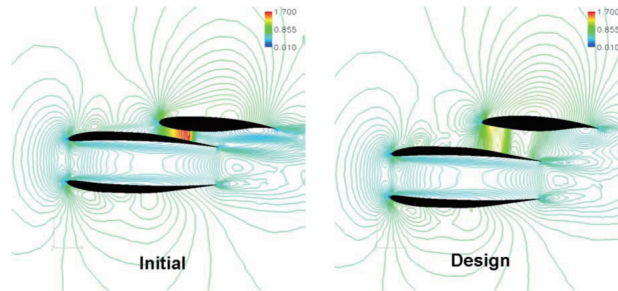Fig. 12. Dual-point design results: Mach contours at the low-lift condition (M∞=0.74, C_L=0.14)

Fig. 13. Dual-point design results: Mach contours at the low-lift condition at 34% span section
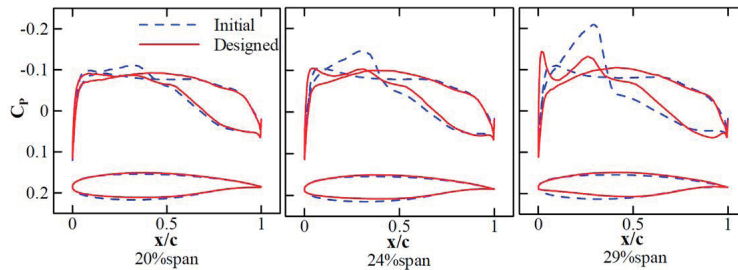

Fig. 14. Dual-point design results: wing section shapes and pressure distributions at the low-lift condition

The design configuration by the dual-point design is a mixed configuration between the low-lift and cruise designs. Wing section shapes particularly have combined characteristics of the single-point design shapes. The low-lift design shape is such that the leading edge becomes sharp and the lower wing surface becomes flat to suppress the strong shock wave on the pylon. On the other side, the cruise design shape is such that the wing upper surface around the mid-chord location moves upward,

which coupled with the nacelle movement, reduces the strength of shock wave on the wing upper surface. Nacelle movement has an important role for the design to reduce the interference effects.

A dual-point design with w=0.3 is also conducted, which results in similar tendency to the design with w=0.5. Fig. 17 shows the pure drag coefficients of design configurations at both conditions. The single-point design at the low-lift condition shows good performance at the low-lift condition
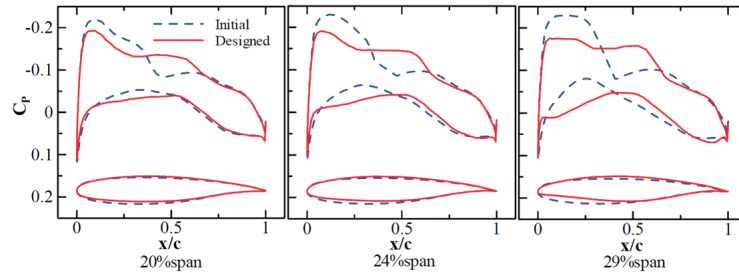
Fig. 15. Dual-point design results: wing section shapes and pressure distributions at the cruise condition
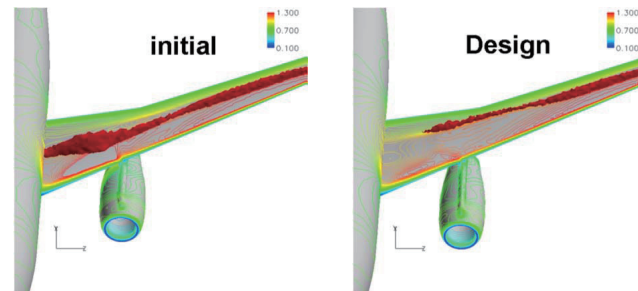

Fig. 16. Dual-point design results: Mach contours and shock visualization at the cruise condition
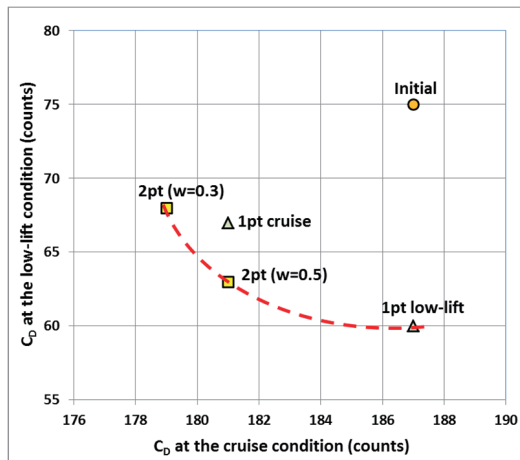

Fig. 17. Design results: Pure drag coefficients at the two design condition

but the performance does not change much at the cruise condition. The design configurations obtained by the single-point low-lift design and the dual-point designs are on the Pareto surface in the drag plot, while the single-point cruise design seems to be stuck at a local minimum.

The downward movement of the nacelle would definitely improve the aerodynamic performances of the configuration by reducing the wing and nacelle interference effects. However, it might cause constraint violation of ground clearance for the nacelle. Also the increased pylon length would increase the structural weight. The viscous drag would also be slightly increased with the increment of the pylon

surface area. These potential performance deficits might be compensated by remarkably improved aerodynamic performances and reduced buffet risk. Thus, a more comprehensive and practical constraints are required for design of the vertical nacelle movement.

5. Conclusions

We conducted single-point and dual-point design studies at low-lift and cruise conditions for DLR-F6 wing-body-nacelle-pylon configuration to reduce strong interference effects among wing, nacelle and pylon components. Design variables are selected for the inboard wing section shapes, pylon section shapes and vertical movement of the nacelle. Applied was a system of aerodynamic design tools developed by combining the surface mesh movement method and an unstructured CFD code with an optimization technique utilizing adjoint-based gradient calculation. Dual point design configurations have good performance at both flow conditions. At the low-lift condition, the strength of shock was reduced to suppress the buffet. At the cruise condition, the shock strength on the inboard wing upper surface was reduced. Dual-point design has a combined configuration of the two single-point designs. As a future work, we will conduct design optimization of the wing-body-nacelle-pylon configuration taking exhaust jet effect of engine nacelle into consideration.

References

[1] Steger, J. L., Dougherty, F. C. and Benek, J. A., "A Chimera Grid Scheme", *ASME Mini-Symposium on Advanced Grid Generation*, 1982.

[2] Nakahashi, K., Togashi, F. and Sharov, D., "Integrated Boundary Definition Method for Overset Unstructured Grid Approach", *AIAA Journal*, Vol. 38, No. 11, 2000, pp. 2077-2084.

[3] Jameson, A., Martinelli, L. and Haimes, B., "Aerodynamic Shape Optimization of Complete Aircraft Configurations Using Unstructured Grids", *AIAA 2004-0533*, 2004.

[4] Murayama, M., Nakahashi, K. and Matsushima, K., "A Robust Method for Unstructured Volume/Surface Mesh Movement", *Transactions of the Japan Society for Aeronautical and Space Sciences*, Vol. 46, No. 152, 2003, pp. 104-112.

[5] Kim, H. and Nakahashi, K., "Surface Mesh Movement for Aerodynamic Design of Body-Installation Junction", *AIAA Journal*, Vol. 45, No. 5, 2007, pp. 1138-1142.

[6] Jameson, A., *Aerodynamic Shape Optimization Using the Adjoint Method*, Lecture Series, Von Karman Institute for Fluid Dynamics, 2003.

[7] Koc, S., Kim, H. and Nakahashi, K., "Aerodynamic Design of Complex Configurations with Junctions", *Journal of Aircraft*, Vol. 43, No. 6, 2006, pp. 1838-1844.

[8] Yamazaki, W., Matsushima, K. and Nakahashi, K., "Aerodynamic Design Optimization Using the Drag-Decomposition Method", *AIAA J.*, vol. 46, No.4, 2008, pp. 1096-1106.

[9] Kim, H. Sasaki, D., Obayashi, S. and Nakahashi, K., "Aerodynamic Optimization of Supersonic Transport Wing Using Unstructured Adjoint Method", *AIAA Journal*, Vol. 39, No. 6, 2001, pp. 1011-1020.

[10] Kim, H., Koc, S. and Nakahashi, K., "Surface Modification Method for Aerodynamic Design Optimization", *AIAA Journal*, Vol. 43, No. 4, 2005, pp. 727-740.

[11] Nakahashi, K., Ito, Y. and Togashi, F., "Some Challenges of Realistic Flow Simulations by Unstructured Grid CFD", *International Journal for Numerical Methods in Fluids*, Vol. 43, No. 6-7, 2003, pp. 769-783.

[12] Sharov, D. and Nakahashi, K., "Reordering of Hybrid Unstructured Grids for Lower-Upper Symmetric Gauss-Seidel Computations", *AIAA Journal*, Vol. 36, No. 3, 1998, pp. 484-486.

[13] Vanderplaats, G. N., *Numerical Optimization Techniques for Engineering Design: with Applications*, McGraw Hill, N.Y., 1984.

[14] Rossow, C. C., Godard, J. L., Hoheisel, H. and Schmitt, V., "Investigation of Propulsion Integration Interference Effects on a Transport Aircraft Configuration", *Journal of Aircraft*, Vol. 31, No. 5, 1994, pp. 1022-1030.

[15] Ito, Y. and Nakahashi, K., "Direct Surface Triangulation Using Stereolithography Data", *AIAA Journal*, Vol. 40, No. 3, 2002, pp. 490-496.

[16] Sharov, D. and Nakahashi, K., "A Boundary Recovery Algorithm for Delaunay Tetrahedral Meshing", *5th International Conference On Numerical Grid Generation in Computational Field Simulations*, 1996, pp. 229-238.

[17] Kim, H., Obayashi, S. and Nakahashi, K., "Flap-Deflection Optimization for Transonic Cruise Performance Improvement of Supersonic Transport Wing", *Journal of Aircraft*, Vol. 38, No. 4, 2001, pp. 709-717.

[18] Hicks, R. M. and Henne, P. A., "Wing Design by Numerical Optimization", *Journal of Aircraft*, Vol. 15, No. 7, 1978, pp. 407-412.